First all-flavor neutrino pointlike source search with the ANTARES neutrino telescope

A. Albert,[1] M. André,[2] M. Anghinolfi,[3] G. Anton,[4] M. Ardid,[5] J.-J. Aubert,[6] T. Avgitas,[7] B. Baret,[7] J. Barrios-Martí,[8,*] S. Basa,[9] B. Belhorma,[10] V. Bertin,[6] S. Biagi,[11] R. Bormuth,[12,13] S. Bourret,[7] M. C. Bouwhuis,[12] H. Brânzaş,[14] R. Bruijn,[12,15] J. Brunner,[6] J. Busto,[6] A. Capone,[16,17] L. Caramete,[14] J. Carr,[6] S. Celli,[16,17,18] R. Cherkaoui El Moursli,[19] T. Chiarusi,[20] M. Circella,[21] J. A. B. Coelho,[7] A. Coleiro,[7,8] R. Coniglione,[11] H. Costantini,[6] P. Coyle,[6] A. Creusot,[7] A. F. Díaz,[22] A. Deschamps,[23] G. De Bonis,[17] C. Distefano,[11] I. Di Palma,[16,17] A. Domi,[3,24] C. Donzaud,[7,25] D. Dornic,[6] D. Drouhin,[1] T. Eberl,[4] I. El Bojaddaini,[26] N. El Khayati,[19] D. Elsässer,[27] A. Enzenhöfer,[6] A. Ettahiri,[19] F. Fassi,[19] I. Felis,[5] L. A. Fusco,[20,28] S. Galatà,[7] P. Gay,[29,7] V. Giordano,[30] H. Glotin,[31,32] T. Grégoire,[7] R. Gracia Ruiz,[7] K. Graf,[4] S. Hallmann,[4] H. van Haren,[33] A. J. Heijboer,[12] Y. Hello,[23] J. J. Hernández-Rey,[8] J. Hößl,[4] J. Hofestädt,[4] C. Hugon,[3,24] G. Illuminati,[8] C. W. James,[4] M. de Jong,[12,13] M. Jongen,[12] M. Kadler,[27] O. Kalekin,[4] U. Katz,[4] D. Kießling,[4] A. Kouchner,[7,32] M. Kreter,[27] I. Kreykenbohm,[34] V. Kulikovskiy,[6,35] C. Lachaud,[7] R. Lahmann,[4] D. Lefèvre,[36] E. Leonora,[30,37] M. Lotze,[8] S. Loucatos,[38,7] M. Marcelin,[9] A. Margiotta,[20,28] A. Marinelli,[39,40] J. A. Martínez-Mora,[5] R. Mele,[41,42] K. Melis,[12,15] T. Michael,[12] P. Migliozzi,[41] A. Moussa,[26] S. Navas,[43] E. Nezri,[9] M. Organokov,[44] G. E. Păvălaş,[14] C. Pellegrino,[20,28] C. Perrina,[16,17] P. Piattelli,[11] V. Popa,[14] T. Pradier,[44] L. Quinn,[6] C. Racca,[1] G. Riccobene,[11] A. Sánchez-Losa,[21] M. Saldaña,[5] I. Salvadori,[6] D. F. E. Samtleben,[12,13] M. Sanguineti,[3,24] P. Sapienza,[11] F. Schüssler,[38] C. Sieger,[4] M. Spurio,[20,28] Th. Stolarczyk,[38] M. Taiuti,[3,24] Y. Tayalati,[19] A. Trovato,[11] D. Turpin,[6] C. Tönnis,[8] B. Vallage,[38,7] V. Van Elewyck,[7,32] F. Versari,[20,28] D. Vivolo,[41,42] A. Vizzoca,[16,17] J. Wilms,[34] J. D. Zornoza,[8] and J. Zúñiga[8]

(ANTARES Collaboration)

[1]*GRPHE—Université de Haute Alsace—Institut universitaire de technologie de Colmar, 34 rue du Grillenbreit BP 50568–68008 Colmar, France*
[2]*Technical University of Catalonia, Laboratory of Applied Bioacoustics, Rambla Exposició, 08800 Vilanova i la Geltrú, Barcelona, Spain*
[3]*INFN—Sezione di Genova, Via Dodecaneso 33, 16146 Genova, Italy*
[4]*Friedrich-Alexander-Universität Erlangen-Nürnberg, Erlangen Centre for Astroparticle Physics, Erwin-Rommel-Str. 1, 91058 Erlangen, Germany*
[5]*Institut d'Investigació per a la Gestió Integrada de les Zones Costaneres (IGIC)—Universitat Politècnica de València. C/Paranimf 1, 46730 Gandia, Spain*
[6]*Aix Marseille Univ, CNRS/IN2P3, CPPM, Marseille, France*
[7]*APC, Univ Paris Diderot, CNRS/IN2P3, CEA/Irfu, Obs de Paris, Sorbonne Paris Cité, France*
[8]*IFIC—Instituto de Física Corpuscular (CSIC—Universitat de València) c/ Catedrático José Beltrán, 2 E-46980 Paterna, Valencia, Spain*
[9]*LAM—Laboratoire d'Astrophysique de Marseille, Pôle de l'Étoile Site de Château-Gombert, rue Frédéric Joliot-Curie 38, 13388 Marseille Cedex 13, France*
[10]*National Center for Energy Sciences and Nuclear Techniques, B.P.1382, R. P.10001 Rabat, Morocco*
[11]*INFN—Laboratori Nazionali del Sud (LNS), Via S. Sofia 62, 95123 Catania, Italy*
[12]*Nikhef, Science Park, Amsterdam, The Netherlands*
[13]*Huygens-Kamerlingh Onnes Laboratorium, Universiteit Leiden, The Netherlands*
[14]*Institute for Space Science, RO-077125 Bucharest, Măgurele, Romania*
[15]*Universiteit van Amsterdam, Instituut voor Hoge-Energie Fysica, Science Park 105, 1098 XG Amsterdam, The Netherlands*
[16]*INFN—Sezione di Roma, P.le Aldo Moro 2, 00185 Roma, Italy*
[17]*Dipartimento di Fisica dell'Università La Sapienza, P.le Aldo Moro 2, 00185 Roma, Italy*
[18]*Gran Sasso Science Institute, Viale Francesco Crispi 7, 00167 'Aquila, Italy*
[19]*University Mohammed V in Rabat, Faculty of Sciences, 4 av. Ibn Battouta, B.P. 1014, R.P. 10000*
[20]*INFN—Sezione di Bologna, Viale Berti-Pichat 6/2, 40127 Bologna, Italy*
[21]*INFN—Sezione di Bari, Via E. Orabona 4, 70126 Bari, Italy*
[22]*Department of Computer Architecture and Technology/CITIC, University of Granada, 18071 Granada, Spain*
[23]*Géoazur, UCA, CNRS, IRD, Observatoire de la Côte d'Azur, Sophia Antipolis, France*
[24]*Dipartimento di Fisica dell'Università, Via Dodecaneso 33, 16146 Genova, Italy*
[25]*Université Paris-Sud, 91405 Orsay Cedex, France*
[26]*University Mohammed I, Laboratory of Physics of Matter and Radiations, B.P.717, Oujda 6000, Morocco*

[27]*Institut für Theoretische Physik und Astrophysik, Universität Würzburg, Emil-Fischer Str. 31, 97074 Würzburg, Germany*
[28]*Dipartimento di Fisica e Astronomia dell'Università, Viale Berti Pichat 6/2, 40127 Bologna, Italy*
[29]*Laboratoire de Physique Corpusculaire, Clermont Université, Université Blaise Pascal, CNRS/IN2P3, BP 10448, F-63000 Clermont-Ferrand, France*
[30]*INFN—Sezione di Catania, Viale Andrea Doria 6, 95125 Catania, Italy*
[31]*LSIS, Aix Marseille Université CNRS ENSAM LSIS UMR 7296 13397 Marseille, France; Université de Toulon CNRS LSIS UMR 7296, 83957 La Garde, France*
[32]*Institut Universitaire de France, 75005 Paris, France*
[33]*Royal Netherlands Institute for Sea Research (NIOZ), Landsdiep 4, 1797 SZ 't Horntje (Texel), The Netherlands*
[34]*Dr. Remeis-Sternwarte and ECAP, Universität Erlangen-Nürnberg, Sternwartstr. 7, 96049 Bamberg, Germany*
[35]*Moscow State University, Skobeltsyn Institute of Nuclear Physics, Leninskie gory, 119991 Moscow, Russia*
[36]*Mediterranean Institute of Oceanography (MIO), Aix-Marseille University, 13288, Marseille, Cedex 9, France; Université du Sud Toulon-Var, CNRS-INSU/IRD UM 110, 83957, La Garde Cedex, France*
[37]*Dipartimento di Fisica ed Astronomia dell'Università, Viale Andrea Doria 6, 95125 Catania, Italy*
[38]*Direction des Sciences de la Matière—Institut de recherche sur les lois fondamentales de l'Univers—Service de Physique des Particules, CEA Saclay, 91191 Gif-sur-Yvette Cedex, France*
[39]*INFN—Sezione di Pisa, Largo B. Pontecorvo 3, 56127 Pisa, Italy*
[40]*Dipartimento di Fisica dell'Università, Largo B. Pontecorvo 3, 56127 Pisa, Italy*
[41]*INFN—Sezione di Napoli, Via Cintia 80126 Napoli, Italy*
[42]*Dipartimento di Fisica dell'Università Federico II di Napoli, Via Cintia 80126, Napoli, Italy*
[43]*Dpto. de Física Teórica y del Cosmos & C.A.F.P.E., University of Granada, 18071 Granada, Spain*
[44]*Université de Strasbourg, CNRS, IPHC UMR 7178, F-67000 Strasbourg, France*
(Received 6 June 2017; published 3 October 2017)

A search for cosmic neutrino sources using the data collected with the ANTARES neutrino telescope between early 2007 and the end of 2015 is performed. For the first time, all neutrino interactions—charged- and neutral-current interactions of all flavors—are considered in a search for point-like sources with the ANTARES detector. In previous analyses, only muon neutrino charged-current interactions were used. This is achieved by using a novel reconstruction algorithm for shower-like events in addition to the standard muon track reconstruction. The shower channel contributes about 23% of all signal events for an E^{-2} energy spectrum. No significant excess over background is found. The most signal-like cluster of events is located at $(\alpha, \delta) = (343.8°, 23.5°)$ with a significance of 1.9σ. The neutrino flux sensitivity of the search is about $E^2 d\Phi/dE = 6 \times 10^{-9}$ GeV cm^{-2} s^{-1} for declinations from $-90°$ up to $-42°$, and below 10^{-8} GeV cm^{-2} s^{-1} for declinations up to 5°. The directions of 106 source candidates and 13 muon track events from the IceCube high-energy sample events are investigated for a possible neutrino signal and upper limits on the signal flux are determined.

DOI: 10.1103/PhysRevD.96.082001

I. INTRODUCTION

Different types of astrophysical objects have been proposed as production sites of high-energy neutrinos through the decay of charged pions, previously produced in the interactions of nuclei with ambient matter or radiation [1–5]. In contrast to charged cosmic rays, neutrinos are not deflected by (inter)galactic magnetic fields and point straight back to their production sites. Finding sources of cosmic neutrinos would identify sources of cosmic rays, whose origin and acceleration processes are a long-standing astrophysical question. The results of the latest search for point-like sources using the ANTARES neutrino telescope are presented in this paper. For the first time, events based on the signal induced by electromagnetic and/or hadronic showers are included. This has been achieved by using a new reconstruction algorithm [6,7] which allows a median pointing accuracy between 2° and 3° for electron neutrinos which interact via charged currents (CC) with energies in the 10^3–10^3 GeV range.

This paper is structured as follows. In Sec. II the ANTARES neutrino telescope and the event selection for this analysis are introduced. The search method is

*Corresponding author.
javier.barrios@ific.uv.es

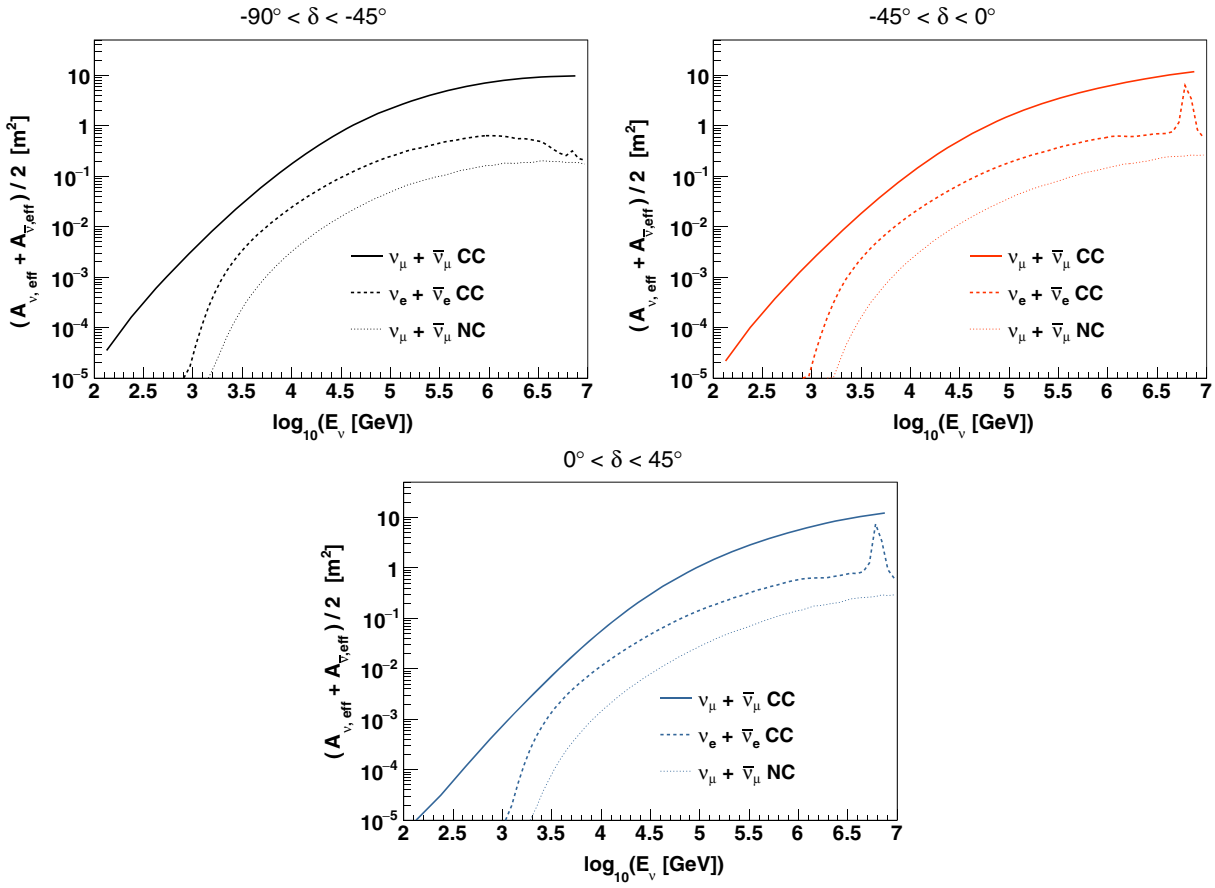

FIG. 1. Effective area for $\nu_\mu + \bar{\nu}_\mu$ CC events after the track selection cuts (solid line) and for $\nu_e + \bar{\nu}_e$ CC and $\nu_\mu + \bar{\nu}_\mu$ NC events after the shower selection cuts (dashed lines) considering three declination ranges.

explained in Sec. III, the results of the analysis are shown in Sec. IV, and the possible effects due to systematic uncertainties are discussed in Sec. V. Finally, the conclusions are summarized in Sec. VI.

II. ANTARES NEUTRINO TELESCOPE AND EVENT SELECTION

The ANTARES telescope [8], located in the Mediterranean Sea, is the largest neutrino detector in the Northern Hemisphere. The detector comprises a three-dimensional array of 885 optical modules (OMs), each one housing a 10-in photomultiplier tube (PMT), and distributed over 12 vertical strings anchored at the sea floor at a depth of about 2400 m. The detection of light from up-going charged particles is optimized with the PMTs facing 45° downward.

Simulations are used to evaluate the performance of the detector. Atmospheric muons and neutrinos are simulated with the MUPAGE [9,10] and GENHEN [11,12] packages, respectively. For the simulation of atmospheric muons, the total amount of simulated events corresponds to 1/3 of the total live time of the data set. The Bartol flux [13] is considered to represent the atmospheric neutrino flux. The simulation of the amount of optical background (^{40}K and bioluminescence) is performed according to the collected data in order to account for the variations of the environmental conditions [14].

The data used for the analysis was recorded between January 29, 2007 and December 31, 2015. During this period, which includes the commissioning phase, the detector operation with at least five lines corresponds to a total live time of 2423.6 days. The event selection is optimized following a blind procedure on pseudodata sets of data randomized in time (pseudoexperiments) before performing the analysis. A more detailed description of the pseudoexperiments can be seen in Sec. III D. The selection criteria for tracks and showers are explained in Secs. II A and II B, respectively. These criteria have been optimized to minimize the neutrino flux needed for a 5σ discovery of a point-like source in 50% of the pseudoexperiments. The effective area for $\overset{(-)}{\nu}_\mu$[1] CC after the track selection cuts, and for, $\overset{(-)}{\nu}_e$ CC and $\overset{(-)}{\nu}_\mu$ neutral-current (NC) events after the shower selection cuts can be seen in Fig. 1.

[1]The notation, $\overset{(-)}{\nu}$ refers to both neutrinos and antineutrinos.

TABLE I. Selection cuts for the track sample and number of remaining simulated events after each step for atmospheric muons ($n_\mu^{\rm atm}$), atmospheric neutrinos ($n_\nu^{\rm atm}$), and cosmic neutrinos ($n_\nu^{E^{-2}}$) reconstructed as a track in the detector. For cosmic neutrinos, a flux according to $d\Phi/dE = 10^{-8}(E/\mathrm{GeV})^{-2}\ \mathrm{GeV}^{-1}\,\mathrm{cm}^{-2}\,\mathrm{s}^{-1}$ is assumed.

Criterion	Condition	$n_\mu^{\rm atm}$	$n_\nu^{\rm atm}$	$n_\nu^{E^{-2}}$
Trigger		4.9×10^8	6.3×10^4	204
Upgoing	$\cos\theta_{tr} > -0.1$	4.3×10^7	5.0×10^4	151
Angular error estimate	$\beta_{tr} < 1°$	2.2×10^7	3.3×10^4	105
Track reconstruction quality	$\Lambda > -5.2$	1513	7475	44
Track length and energy cut	$L_\mu > 380$ m, $\log_{10}(\rho) > 1.6$	1117	7086	41

The simulations produced to account for the interaction of $\overset{(-)}{\nu}_\tau$ cover a limited live time of the data. Because of this, the contribution due to the leptonic and hadronic channels after the interaction of $\overset{(-)}{\nu}_\tau$ are estimated by scaling the contribution of other flavor neutrino events. A neutrino flux with an E^{-2} energy is assumed in this scaling. The obtained rates are the following: to take into account the decay of the outgoing τ into a μ (branching ratio of ∼17%) after a $\overset{(-)}{\nu}_\tau$ CC interaction, the number of events predicted by CC $\overset{(-)}{\nu}_\mu$ interactions is increased by 9%; to take into account the decay of the outgoing τ into an electron (branching ratio of ∼17%), the number of CC $\overset{(-)}{\nu}_e$ is increased by 12%; finally, to take into account the τ decaying into hadrons (branching ratio of ∼64%) after a $\overset{(-)}{\nu}_\tau$ CC interaction and the $\overset{(-)}{\nu}_\tau$ NC interactions, the small number of events predicted by $\overset{(-)}{\nu}_\mu$ NC interactions is increased by 374%.

A. Muon track selection

Muon tracks are reconstructed using a multistep procedure that concludes with a maximum likelihood method [15]. This likelihood takes into account the so-called *hits*. A hit is defined as the digital information on the time and amplitude of a PMT signal, where the latter is proportional to the number of detected photons. As in the previous publication [16], muon events are selected by applying cuts on the reconstructed zenith angle ($\cos\theta_{tr} > -0.1$), the estimated angular error ($\beta_{tr} < 1°$), and the parameter that describes the quality of the reconstruction ($\Lambda > -5.2$). An approximated evaluation of the energy deposited per unit of path length is used to estimate the muon energy. An energy estimator ρ is defined using the hit charge (recorded by all PMTs used to reconstruct the track) and the length of the muon path in the detector [17,18]. The energy estimator fails for events for which the muon energy is below the value of the critical energy to produce significant energy losses due to radiative processes (∼500 GeV), and for tracks with an estimated track length L_μ below 380 m, yielding small values of ρ. Such events are excluded from the analysis. Table I gives an overview of the selection cuts applied for the simulated track sample. A total of 7622 neutrino candidates in the track channel are selected in data for this search.

B. Shower selection

Shower events are reconstructed with a new algorithm based on a two-step procedure. In the first step, the interaction vertex is obtained by the maximization of an M-estimator $M_{\rm est}$, which depends on the time and charge of the hits. The direction of the event is estimated with a maximum likelihood method, using the information of the reconstructed interaction vertex and the detected amplitude of the OMs. Shower events are required to be reconstructed as up-going or coming from close to the horizon ($\cos\theta_{sh} > -0.1$) with a restriction on the angular error estimate ($\beta_{sh} < 30°$). The interaction vertex of each event is also required to be reconstructed inside or close to the instrumented volume. To further reduce the background from misreconstructed atmospheric muons, additional selection cuts are imposed. These cuts are based on the $M_{\rm est}$ value, on a random decision forest classifier value RDF (made with parameters provided by an alternative shower reconstruction [19]), and on a likelihood $\mathcal{L}_\mu$ (or muon likelihood) that uses information about the hits in the event. A description of these cuts is given in the Appendix. Events passing the muon track selection are excluded from the shower channel, making the two samples mutually exclusive. The full list of selection cuts is summarized in Table II. The selection yields 180 shower events.

C. Comparison between data and simulations

The left side of Fig. 2 compares the distributions of the quality parameter Λ for different types of simulated events with the data set for the track channel. The right side of Fig. 2 shows the comparison at the reconstructed zenith angle for the shower channel. It is estimated that about 13% of the selected muon tracks and 52% of the selected shower events are atmospheric muons misreconstructed as up-going. The simulation overestimates the number of events by 8% (17%) in the track (shower) channel for the final set of cuts. This difference is well within the overall systematic

TABLE II. Selection cuts for the shower sample and number of remaining simulated events after each step for atmospheric muons ($n_\mu^{\rm atm}$), atmospheric neutrinos ($n_\nu^{\rm atm}$), and cosmic neutrinos ($n_\nu^{E^{-2}}$) reconstructed as a shower in the detector. For cosmic neutrinos, a flux according to $d\Phi/dE = 10^{-8}\ (E/\mathrm{GeV})^{-2}\ \mathrm{GeV}^{-1}\,\mathrm{cm}^{-2}\,\mathrm{s}^{-1}$ is assumed. See the Appendix for more details.

Criterion	Condition	$n_\mu^{\rm atm}$	$n_\nu^{\rm atm}$	$n_\nu^{E^{-2}}$
Track Veto	not selected as muon track	4.9×10^8	5.6×10^4	160
Upgoing	$\cos\theta_{sh} > -0.1$	1.5×10^8	2.3×10^4	90
Interaction vertex	$R_{sh} < 300$ m, $\lvert Z_{sh}\rvert < 250$ m	7.7×10^7	2.1×10^4	80
M-estimator	$M_{\rm est} < 1000$	7.2×10^7	2.0×10^4	80
RDF	$RDF > 0.3$	8.0×10^4	2044	24
Muon likelihood	$\mathcal{L}_\mu > 50$	90	109	12

uncertainty on the atmospheric neutrino flux normalization [18]. A larger overestimation of events is observed in the region where the background of misreconstructed atmospheric muons is dominant. On the other hand, in the cascade channel, an underestimation of events is observed for zenith angles larger than $\cos(\theta_{sh}) > 0.4$, which can be explained due to the large uncertainties of the atmospheric neutrino flux. Compared to other searches, the searches for an excess from a point-like direction in the sky are less influenced by higher levels of background contamination. Referring to the right panel of Fig. 2, even if there is a large contamination of atmospheric muons between −0.1 and 0.1, according to our pseudoexperiment simulations the current event selection produces better sensitivities compared to considering only events with $\cos(\theta_{sh}) > 0.1$. A global good agreement between data and Monte Carlo justifies the procedure to optimize the selection criteria for the separation of signal and background using simulated events.

III. SEARCH METHOD

While atmospheric neutrino events are randomly distributed, neutrinos from point-like sources are expected to accumulate in spatial clusters. To find these clusters, a maximum likelihood ratio approach is followed. The

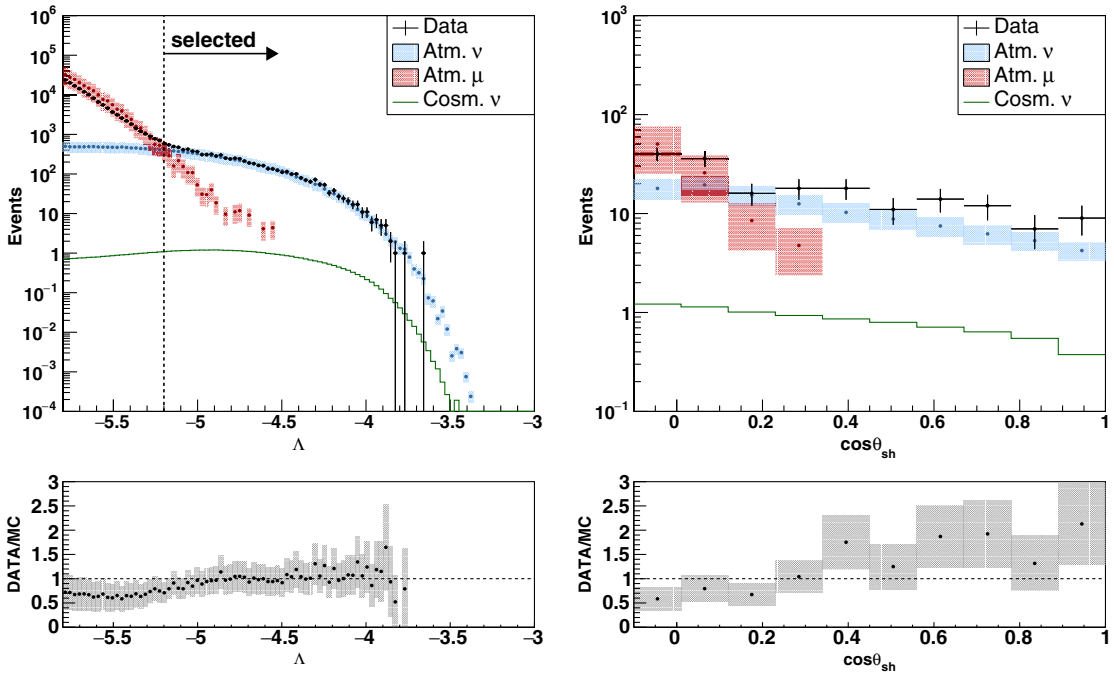

FIG. 2. Left: Comparison of the data with Monte Carlo (MC) simulations as a function of the quality parameter Λ. This figure corresponds to the event distribution after a cut on the estimated angular error ($\beta_{tr} < 1°$) and on the reconstructed zenith angle ($\cos\theta_{tr} > -0.1$). The dashed vertical line marks the cut value. Right: Comparison of the data with the simulations at the zenith θ_{sh} of the reconstructed shower direction. This figure corresponds to the event distribution after all shower selection cuts presented in Table II. For the cosmic neutrinos, a flux according to $d\Phi/dE = 10^{-8}\ (E/\mathrm{GeV})^{-2}\ \mathrm{GeV}^{-1}\,\mathrm{cm}^{-2}\,\mathrm{s}^{-1}$ is assumed in both figures. The two bottom plots show the data-to-MC ratio, where the number of MC events is the sum of atmospheric muons and neutrinos.

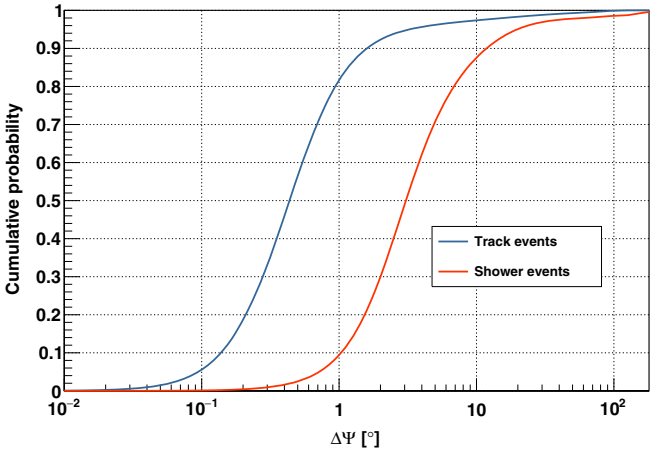

FIG. 3. Probability to obtain a reconstructed angle within $\Delta\Psi$ between the reconstructed direction of track-like events (blue) and shower-like events (red) with respect to the true Monte Carlo neutrino direction. A neutrino flux with an E^{-2} energy spectrum is assumed.

likelihood used describes the data in terms of signal and background probability density functions (PDFs) and is defined as

$$\log \mathcal{L}_{\mathrm{s+b}} = \sum_{\mathcal{S}} \sum_{i \in \mathcal{S}} \log\left[\mu^{\mathcal{S}}_{\mathrm{sig}} \mathcal{F}^{\mathcal{S}}_{i} \mathcal{P}^{\mathcal{S}}_{\mathrm{sig,i}} + \mathcal{N}^{\mathcal{S}} \mathcal{B}^{\mathcal{S}}_{i} \mathcal{P}^{\mathcal{S}}_{\mathrm{bkg,i}}\right] - \mu_{\mathrm{sig}}. \tag{1}$$

In this equation, $\mathcal{S}$ denotes the sample (tr for tracks, sh for showers), i indicates the event of the sample $\mathcal{S}$, $\mu^{\mathcal{S}}_{\mathrm{sig}}$ is the number of signal events fitted to in the $\mathcal{S}$ sample, $\mathcal{F}^{\mathcal{S}}_{i}$ is a parametrization of the point-spread function, $\mathcal{P}^{\mathcal{S}}_{\mathrm{sig,i}}$ is derived from the probability density function of the energy estimator (yielding the probability of measuring the signal with the reconstructed energy of the event i), $\mathcal{N}^{\mathcal{S}}$ is the total number of events in the $\mathcal{S}$ sample, $\mathcal{B}^{\mathcal{S}}_{i}$ is the background rate obtained from the distribution of the observed background events at the declination of event i, $\mathcal{P}^{\mathcal{S}}_{\mathrm{bkg,i}}$ is the probability density function of the energy estimator for background, and $\mu_{\mathrm{sig}} = \mu^{tr}_{\mathrm{sig}} + \mu^{sh}_{\mathrm{sig}}$ is the total number of fitted signal events. More details on the components of the PDFs are given below.

A. Point-spread function

The distribution of signal events around a hypothetical point-like source is described by the point-spread function (PSF) $\mathcal{F}$. The PSF is defined as the probability density to find a reconstructed event at an angular distance $\Delta\Psi$ around the direction of the source. It depends on the angular resolution of the event sample. Figure 3 shows the cumulative distributions of the angular distance between the reconstructed and true neutrino direction for track and shower events. The PSFs are determined from Monte Carlo simulations of neutrinos with an E^{-2} energy spectrum. The figure shows that about 50% of the track (shower) events are reconstructed within 0.4° (3°) of the parent neutrino.

B. Background rate

The background rate $\mathcal{B}$ is described as a function of the declination δ. Given the small expected contribution of a cosmic signal in the overall data set, the background rate is estimated directly from the measured data. Due to the Earth's rotation and a sufficiently uniform exposure, the background is considered independent of right ascension α. The rate of selected events as a function of declination is shown in Fig. 4.

C. Energy estimator

Neutrinos generated in the atmosphere have a much softer energy spectrum ($\propto E^{-3.7}$) than neutrinos from the expected astrophysical flux proportional to E^{-2}. For this reason, the energy estimator information is used in the likelihood to further distinguish between cosmic signal and atmospheric background.

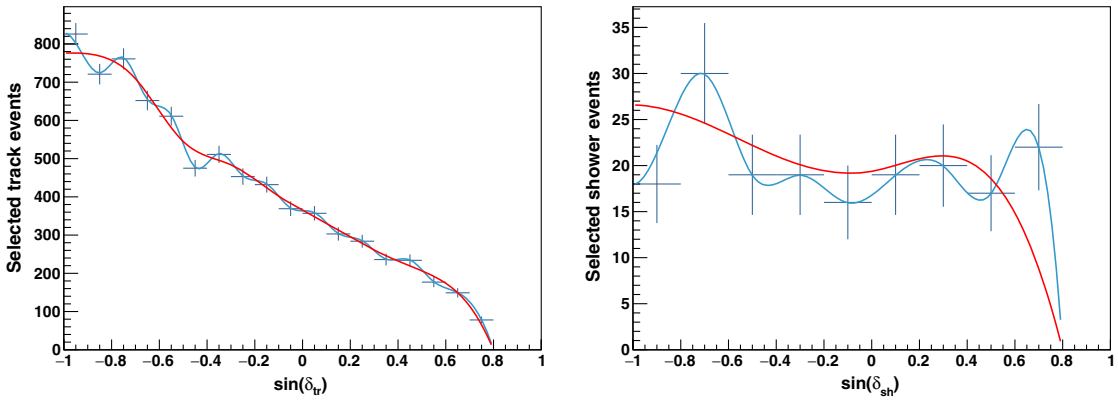

FIG. 4. Number of selected track-like (left) and shower-like (right) events as a function of the reconstructed declination. The red and blue lines are different spline parametrizations (see Sec. V). The different shape for showers is mainly due to a higher relative contamination of atmospheric muons in the sample.

For the shower channel, the number of hits (N_{sh}) used by the reconstruction algorithm is employed as the energy estimator.

A different and more elaborate approach is assumed for the track channel. In this case the estimator ρ is used as a proxy for the energy of the neutrino event. The information of the event angular error estimate β_{tr} is also included. Moreover, the dependence of the energy estimator on the declination of the event is taken into account by generating both the signal and background PDFs in steps of 0.2 over $\sin\delta$.

D. Implementation

The significance of any observation is determined by a test statistic denoted as $\mathcal{Q}$ which is defined from the likelihood as

$$\mathcal{Q} = \log \mathcal{L}_{\mathrm{s+b}} - \log \mathcal{L}_{\mathrm{b}}. \tag{2}$$

The $\mathcal{Q}$ distributions for different signal strengths are determined from pseudoexperiments. In these, $O(10^4$–$10^5)$ random sky maps are generated with a number of background events that follow the declination-dependent event distribution as seen in the actual data, and a uniform right ascension. In addition, signal events are injected according to the investigated spectrum by assuming either a point or extended source profile. In Eq. (2) $\mathcal{L}_{\mathrm{b}}$ corresponds to the definition of $\mathcal{L}_{\mathrm{s+b}}$ in Eq. (1) evaluated with the same parameters as the maximum likelihood estimate but with the number of signal events set to zero: $\mu^{\mathrm{tr}}_{\mathrm{sig}} = \mu^{\mathrm{sh}}_{\mathrm{sig}} = 0$ (background-only case).

In the likelihood maximization, the position in the sky of the fitted source is either kept fixed or allowed to be fitted within specific limits depending on the type of search (see Sec. IV). Furthermore, the values of $\mu^{\mathrm{tr}}_{\mathrm{sig}}$ and $\mu^{\mathrm{sh}}_{\mathrm{sig}}$ are left free to vary, and can indeed go below zero to reflect the degree of absence of events around the probed coordinates. The declination-dependent acceptance for a given sample $A_S(\delta)$ is defined as the proportionality constant between a given flux normalization $\Phi_0 = E^2 d\Phi/dE$ and the expected number of signal events for this particular flux. It can be expressed in terms of the effective area, $\mathcal{A}_{\mathrm{eff},S}(E_\nu, \delta)$:

$$A_S(\delta) = \Phi_0^{-1} \iint dt dE_\nu \mathcal{A}_{\mathrm{eff},S}(E_\nu, \delta) \frac{d\Phi}{dE_\nu}, \tag{3}$$

where the integral is over the live time of all selected runs (2423.6 days) and over an energy range large enough to include all potential events within the sensitivity of ANTARES. With the assumed E^{-2} spectrum, 90% of the events are found in an energy range between 2×10^3 and 3×10^6 GeV for the track channel (between 5×10^3 and 4×10^6 GeV for the shower channel). Figure 5 shows how the acceptances for tracks and showers depend on the declination.

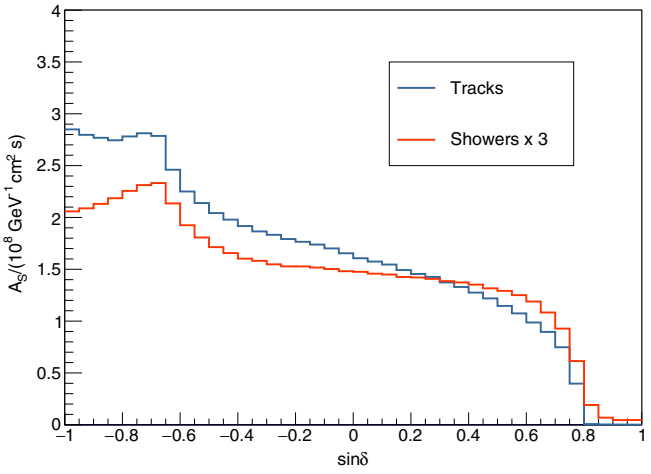

FIG. 5. The acceptance as a function of the source declination for an E^{-2} energy spectrum with a flux normalization factor of $\Phi_0 = 10^{-8}$ GeV cm^{-2} s^{-1} for the track (blue) and shower (red) samples. For better visibility, the acceptance for showers is scaled up by a factor of 3.

IV. SEARCH FOR NEUTRINO SOURCES

The search for astrophysical neutrino sources presented in this paper is performed with four approaches.

(1) *Full sky search*: In the first method, the whole visible sky of ANTARES is scanned in an unbinned way to search for spatial clustering of events with respect to the expected background.

(2) *Candidate list search*: In the second approach, the directions of a predefined list of known objects which are neutrino source candidates are investigated to look for an excess or (in the case of null observation) to determine an upper limit on their neutrino fluxes.

(3) *Galactic Center region*: The third search is similar to the full sky search but is restricted to a region centered at the origin of the Galactic coordinate system $(\alpha, \delta) = (266.40°, -28.94°)$ and defined by an ellipse with a semiaxis of 15° in the direction of the Galactic latitude and a semiaxis of 20° in Galactic longitude. The motivation relies on the number of high-energy neutrino events observed by the IceCube (IC) detector [20,21] that appear to cluster in this region. Furthermore, the H.E.S.S. Collaboration recently discovered an accelerator of PeV protons in the Galactic Center [22] that could produce high-energy neutrinos.

(4) *Sagittarius* A*: Finally, the fourth approach tests the location of Sagittarius A* as an extended source by assuming a Gaussian emission profile of various widths.

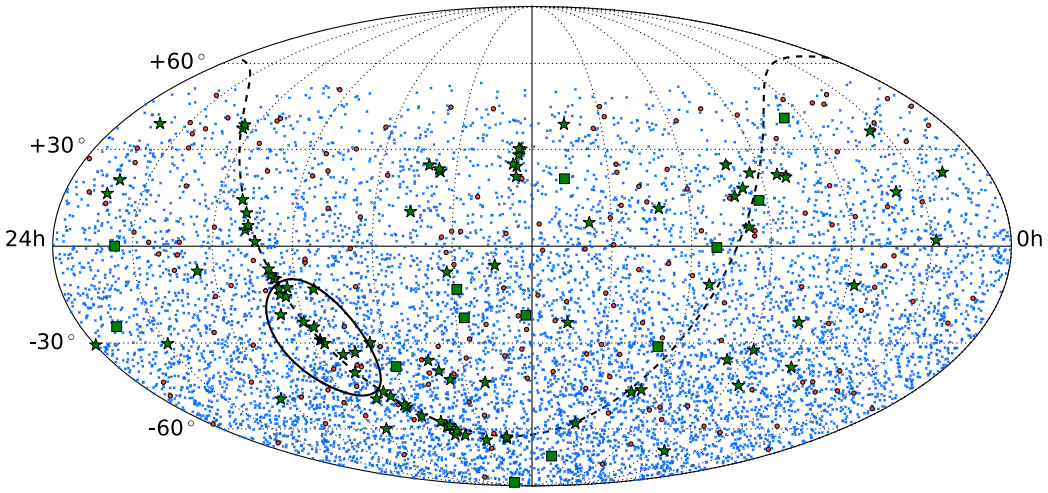

FIG. 6. Sky map in equatorial coordinates of the 7622 track (blue crosses) and 180 shower (red circles) events passing the selection cuts. Yellow stars indicate the location of the 106 candidate neutrino sources, and yellow squares indicate the location of the 13 considered tracks from the IceCube high-energy sample events (HESE) (see Sec. IV B). The black solid ellipse indicates the search region around the Galactic Center, in which the origin of the Galactic coordinates is indicated with a black star. The black dashed line indicates the Galactic equator.

Figure 6 represents the event sample in equatorial coordinates in the ANTARES visible sky. The considered neutrino source candidates and the search region around the Galactic Center are also indicated.

A. Full sky search

In the full sky search, the whole visible sky of ANTARES is divided on a grid with boxes of $1° \times 1°$ in right ascension and declination for the evaluation of the $\mathcal{Q}$-value defined in Eq. (2). This value is maximized in each box by letting the location of the fitted cluster vary freely between the $1° \times 1°$ boundaries. Since an unbinned search is performed, events outside the grid boxes are indeed considered in each $\mathcal{Q}$-value maximization. The pre-trial p-value of each cluster is calculated by comparing the $\mathcal{Q}$-value obtained at the location of the fitted cluster with the background-only $\mathcal{Q}$ obtained from simulations at the corresponding declination. Figure 7 shows the position of the cluster and the pre-trial p-values for all directions in the ANTARES visible sky. The most significant cluster of this search is found at a declination of $\delta = 23.5°$ and a right-ascension of $\alpha = 343.8°$ and with a pre-trial p-value of 3.84×10^{-6}. To account for trial factors, this pre-trial p-value is compared to the distribution of the smallest p-values found anywhere in the sky when performing the same analysis on many pseudodata sets. It is found that 5.9% of pseudoexperiments have a smaller p-value than the one found in the final sample, corresponding to a post-trial significance of 1.9σ (two-sided convention). The upper limit on the neutrino flux coming from this sky location is

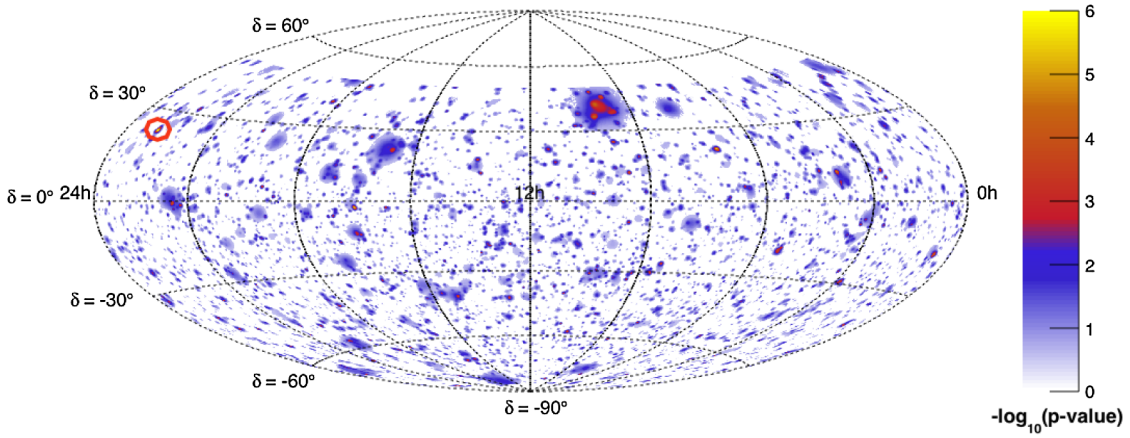

FIG. 7. Sky map in equatorial coordinates of pre-trial p-values for a point-like source of the ANTARES visible sky. The red circle indicates the location of the most significant cluster of the full sky search. For this map, a smaller grid size of $0.2° \times 0.2°$ was used.

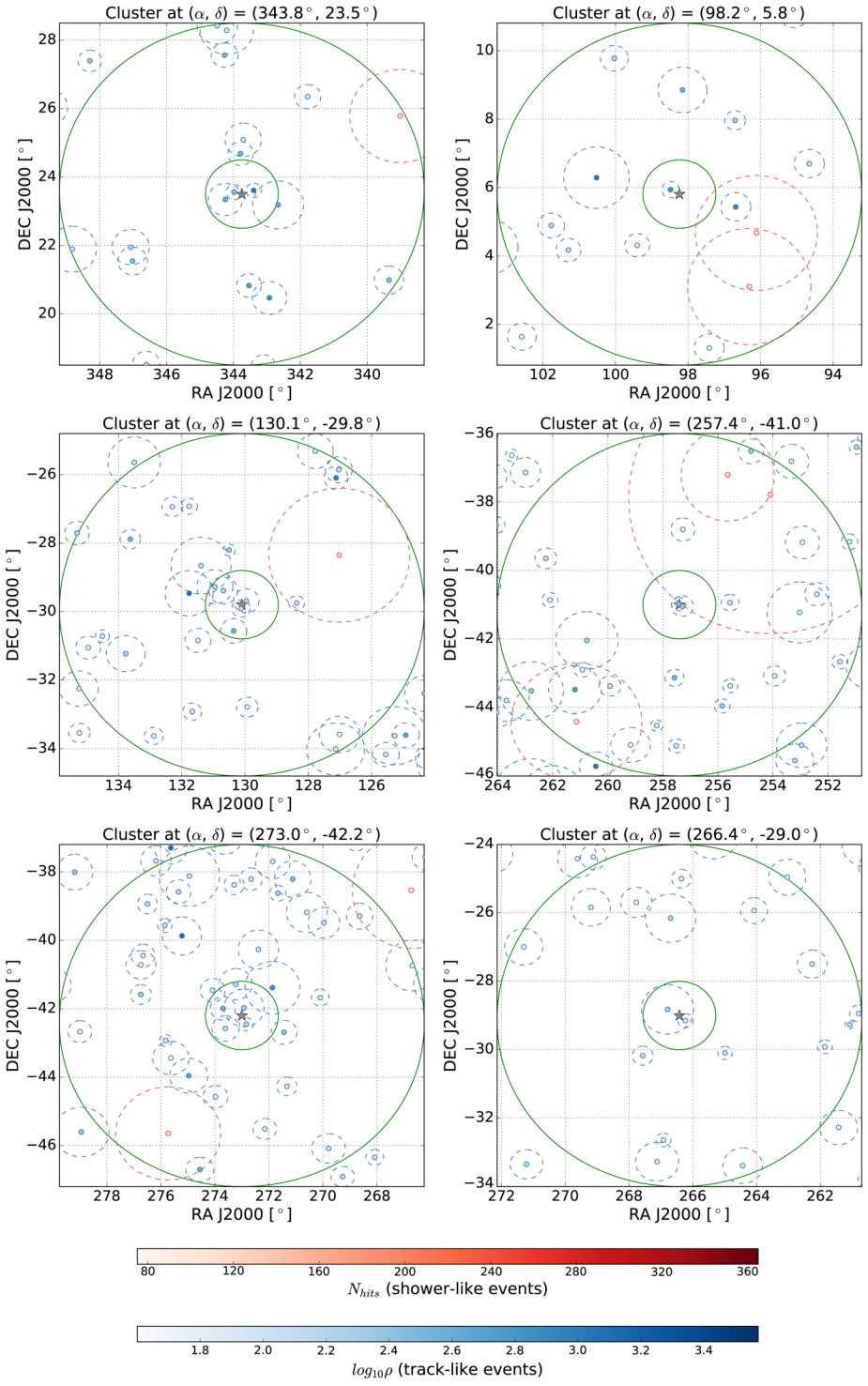

FIG. 8. Distribution of events in the (α, δ) (RA, DEC) coordinates for the most significant clusters found in the full sky search (top left), the candidate list search (HESSJ0632 + 057) (top right), the search over the track events from the IceCube HESE sample (track with ID = 3) (middle left), the search around the Galactic Center for an E^{-2} point-like source (middle right), the search around the Galactic Center for an $E^{-2.5}$ point-like source (bottom left), and the search at the location of Sagittarius A* (bottom right). In all figures, the inner (outer) green line depicts the one (five) degree distance from the position of the best fit or known location, indicated as a gray star. The red points denote shower-like events, whereas the blue points indicate track-like events. Different tones of red and blue correspond to the values assumed by the energy estimators—the number of hits (shower-like events) and the ρ parameter (track-like events)—as shown in the legend. The dashed circles around the events indicate the angular error estimate.

$E^2 d\Phi/dE = 3.8 \times 10^{-8}$ GeV cm^{-2} s^{-1}. The location of this cluster is found at a distance of 1.1° from event ID 3 of the six-year Northern Hemisphere Cosmic Neutrino flux sample of IceCube [23]. A rough estimate of the significance of this coincidence is performed. Twenty-six of these 29 events are found in the declination range between −5° and 30°. The remaining events were excluded since the event density in the selected region is larger, and therefore the estimation is slightly more conservative. By assuming a random distribution of 26 events within this declination range, the probability of a random coincidence within 1° between at least one event and the most significant cluster of the full sky search is ∼1%. The distribution of events of this cluster is shown in the top left panel of Fig. 8. It contains 16(3) tracks within 5°(1°) and one shower event within 5°. The upper limits of the highest significant cluster in bands of 1° in declination at 90% C.L. obtained using the Neyman method [24] are shown in Fig. 9. The limits computed in this analysis are set on the total neutrino flux ($\Phi_{\nu_\mu} + \Phi_{\nu_e} + \Phi_{\nu_\tau}$), assuming equipartition at Earth of the three neutrino flavors.

B. Candidate list

The candidate list used in the last ANTARES point-like source analysis [16] contained neutrino source candidates of both Galactic and extra-Galactic origin listed in the TeVCat catalog [27]. These sources had been observed by gamma-ray experiments before July 2011 in the 0.1–100 TeV energy range and with declinations lower than 20°. Furthermore, since the energy of high-energy gamma rays of extra-Galactic origin can degrade before they reach the Earth, extra-Galactic candidates were also selected among the sources observed by gamma-ray satellites in the 1–100 GeV energy range. This paper updates the neutrino search for the 50 objects considered in Ref. [16] with an additional 56 galactic and extra-Galactic sources. The newly considered sources include those detected in the 0.1–100 TeV energy range by gamma-ray experiments after July 2011 and some bright sources with declinations between 20° and 40° not considered in the past. Additionally, the reconstructed direction of the IceCube multi-PeV track event [23] and the 2HWC sources which are not coincident with any known source [28] have been included. Finally, seven more sources are added: the three blazars with highest intensity observed by the TANAMI Collaboration that coincide with three events from the IceCube HESE sample [29–31], and the four gravitationally lensed flat spectrum radio quasars with the highest magnification factor analyzed in a previous work [32].

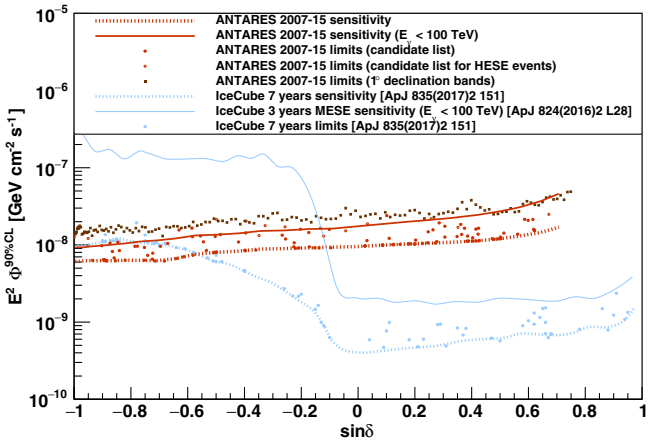

FIG. 9. Upper limits at 90% C.L. on the signal flux from the investigated candidates assuming a E^{-2} spectrum (red circles). The dashed red line shows the ANTARES sensitivity (defined as the median upper limit at 90% C.L. for a background-only case) and the blue dashed line shows the sensitivity of the seven-year point-like source analysis by the IceCube Collaboration for comparison [25]. The upper limits obtained in this analysis are also included (blue dots). The ANTARES 5σ pre-trial discovery flux is a factor 2.5 to 2.9 larger than the sensitivity. The curve for the sensitivity for neutrino energies under 100 TeV is also included (solid red line). The IceCube curve for energies under 100 TeV (solid blue line) is obtained from the three-year Medium Energy Starting Events analysis [26]. The limits of the most significant cluster obtained in bands of 1° in declination (dark red squares) are also shown.

The list of the astronomical candidates is shown in Table III along with their equatorial coordinates, fitted number of signal events, and upper limits on the flux.

The most signal-like cluster is found at the location of HESSJ0632 + 057 at $(\alpha, \delta) = (98.24°, 5.81°)$, with a pre-trial p-value of 0.16%. The second and third most significant sources correspond to PKS1440-389 and PKS0235 + 164, with pre-trial p-values of 0.5% and 5%, respectively. To account for trial factors, the search is performed on the same list of sources using pseudo data sets, from which the distribution of the smallest p-value for a background-only case is obtained. It is found that 13% of the pseudoexperiments have a smaller p-value for any source compared to the one obtained for this location, corresponding to a post-trial significance of 1.5σ (two-sided convention). The cluster contains 11(1) tracks within 5°(1°) and two shower events within 5° around the source candidate. The distribution of events around this source is shown in the top right panel of Fig. 8. The sensitivities and limits calculated with the Neyman method at 90% C.L. and the 5σ discovery flux for this search (assuming a E^{-2} spectrum) are shown in Fig. 9 as a function of the declination. To prevent undesired effects of the Neyman construction [33], the maximum between the sensitivity (i.e., the median upper limit at 90% C.L. for a background-only case) and the limit for the particular location of the source are reported, as is customary in the field [16,25].

The 13 track candidates from the IceCube HESE sample classified as muon tracks [20,21] are considered in a separate candidate list search. Since those events have a

TABLE III. List of astrophysical objects used in the candidate list search. We list the object's coordinates in declination (δ) and right ascension (α). The first column reports the type of source: *Binary* means x-ray binary, *GC* means Galactic Center, *Radio* means radio galaxy, *Sey2* means the Seyfert 2 galaxy, and *UNID* means unidentified. The last two columns show the sum of the fitted number of signal track and shower events $\mu_{\rm sig} = \mu_{\rm sig}^{tr} + \mu_{\rm sig}^{sh}$, and the 90% C.L. upper limits on the flux normalization factor $\Phi_0^{90\%}$ (in units of 10^{-8} GeV cm^{-2} s^{-1}). Candidates of the same type are sorted by declination.

Type	Name	$\delta[^\circ]$	$\alpha[^\circ]$	$\mu_{\rm sig}$	$\Phi_0^{90\%}$	Type	Name	$\delta[^\circ]$	$\alpha[^\circ]$	$\mu_{\rm sig}$	$\Phi_0^{90\%}$
BLLac	PKS2005-489	−48.82	302.37	0.3	0.93		PKS1406-076	−7.90	212.20	–	0.92
	PKS0537-441	−44.08	84.71	0.6	0.96		QSO2022-077	−7.60	306.40	1.0	1.64
	PKS1440-389	−39.14	220.99	2.9	1.56		3C279	−5.79	194.05	0.8	1.59
	PKS0426-380	−37.93	67.17	–	0.70		B1030 + 074	7.19	158.39	–	1.01
	PKS1454-354	−35.67	224.36	1.2	1.28		PKS1502 + 106	10.52	226.10	–	1.03
	TXS1714-336	−33.70	259.40	0.8	1.31		3C454.3	16.15	343.50	–	1.10
	PKS0548-322	−32.27	87.67	–	0.85		4C + 21.35	21.38	186.23	–	1.37
	H2356-309	−30.63	359.78	–	0.79		B1422 + 231	22.93	216.16	–	1.12
	PKS2155-304	−30.22	329.72	–	0.80		PKS1441 + 25	25.03	220.99	–	1.38
	1ES1101-232	−23.49	165.91	–	0.85	Radio	PKS0625-35	−35.49	96.78	–	0.74
	1ES0347-121	−11.99	57.35	–	0.92	SNR	LHA120-N-157B	−69.16	84.43	–	0.63
	RGBJ0152 + 017	1.79	28.17	–	1.14		RCW86	−62.48	220.68	–	0.62
	RBS0723	11.56	131.80	–	1.03		MSH15-52	−59.16	228.53	–	0.68
	PKS0235 + 164	16.61	39.66	2.1	1.93		SNRG327.1-01.1	−55.08	238.65	–	0.63
	RGBJ2243 + 203	20.35	340.98	–	1.29		RXJ0852.0-4622	−46.37	133.00	–	0.65
	VERJ0521 + 211	21.21	80.44	1.2	1.84		RXJ1713.7-3946	−39.75	258.25	–	0.67
	S20109 + 22	22.74	18.02	–	1.30		W28	−23.34	270.43	0.8	1.43
	PKS1424 + 240	23.79	216.75	–	1.12		SNRG015.4 + 00.1	−15.47	274.52	0.2	1.34
	MS1221.8 + 2452	24.61	186.10	–	1.13		W44	1.38	284.04	–	0.97
	1ES0647 + 250	25.05	102.69	–	1.65		HESSJ1912 + 101	10.15	288.21	–	1.03
	S31227 + 25	25.30	187.56	–	1.14		W51C	14.19	290.75	–	1.07
	WComae	28.23	185.38	–	1.20		IC443	22.50	94.21	–	1.12
	1ES1215 + 303	30.10	184.45	–	1.26	Sey2	ESO139-G12	−59.94	264.41	–	0.82
	1ES1218 + 304	30.19	185.36	–	1.21		CentaurusA	−43.02	201.36	–	0.62
	Markarian421	38.19	166.08	–	1.59	UNID	HESSJ1507-622	−62.34	226.72	–	0.62
Binary	CirX-1	−57.17	230.17	–	0.84		HESSJ1503-582	−58.74	226.46	–	0.62
	GX339-4	−48.79	255.70	–	0.63		HESSJ1023-575	−57.76	155.83	1.5	1.08
	LS5039	−14.83	276.56	–	1.19		HESSJ1614-518	−51.82	243.58	0.7	0.96
	SS433	4.98	287.96	–	0.99		HESSJ1641-463	−46.30	250.26	–	0.78
	HESSJ0632 + 057	5.81	98.24	2.7	2.40		HESSJ1741-302	−30.20	265.25	0.6	1.29
FSRQ	S30218 + 35	35.94	35.27	0.7	2.15		HESSJ1826-130	−13.01	276.51	–	1.07
	B32247 + 381	38.43	342.53	–	1.54		HESSJ1813-126	−12.68	273.34	–	0.90
GC	GalacticCentre	−29.01	266.42	1.1	1.36		HESSJ1828-099	−9.99	277.24	0.7	1.45
PWN	HESSJ1356-645	−64.50	209.00	0.4	0.98		HESSJ1834-087	−8.76	278.69	–	0.92
	HESSJ1303-631	−63.20	195.75	–	0.64		2HWCJ1309-054	−5.49	197.31	–	0.92
	HESSJ1458-608	−60.88	224.54	1.2	1.05		2HWCJ1852 + 013*	1.38	283.01	–	0.97
	HESSJ1616-508	−50.97	243.97	0.5	0.96		2HWCJ1902 + 048*	4.86	285.51	–	0.99
	HESSJ1632-478	−47.82	248.04	–	0.73		MGROJ1908 + 06	6.27	286.99	–	1.22
	VelaX	−45.60	128.75	–	0.62		2HWCJ1829 + 070	7.03	277.34	–	1.01
	HESSJ1831-098	−9.90	277.85	–	0.95		2HWCJ1907 + 084*	8.50	286.79	–	1.02
	HESSJ1837-069	−6.95	279.41	–	1.30		ICPeV	11.42	110.63	–	1.03
	MGROJ2019 + 37	36.83	304.64	0.4	2.08		2HWCJ1914 + 117	11.72	288.68	–	1.16
Pulsar	PSRB1259-63	−63.83	195.70	–	0.64		2HWCJ1921 + 131	13.13	290.30	–	1.05
	Terzan5	−24.90	266.95	–	1.09		2HWCJ0700 + 143	14.32	105.12	–	1.48
	Geminga	17.77	98.47	0.9	1.75		VERJ0648 + 152	15.27	102.20	–	1.57
	Crab	22.01	83.63	0.1	1.64		2HWCJ0819 + 157	15.79	124.98	–	1.06
Quasar	PKS1424-418	−42.10	216.98	1.1	1.04		2HWCJ1928 + 177	17.78	292.15	–	1.26
	SwiftJ1656.3-3302	−33.04	254.07	–	1.10		2HWCJ1938 + 238	23.81	294.74	–	1.24
	PKS1622-297	−29.90	246.50	–	0.80		2HWCJ1949 + 244	24.46	297.42	–	1.60
	PKS0454-234	−23.43	74.27	–	0.84		2HWCJ1955 + 285	28.59	298.83	–	1.18
	PKS1830-211	−21.07	278.42	–	0.86		2HWCJ1953 + 294	29.48	298.26	–	1.20
	QSO1730-130	−13.10	263.30	–	0.94		2HWCJ1040 + 308	30.87	160.22	–	1.42
	PKS0727-11	−11.70	112.58	1.3	1.59		2HWCJ2006 + 341	34.18	301.55	–	1.38

TABLE IV. The 13 IceCube muon track candidates from the IceCube HESE sample [20,21] that are in the field of view of the ANTARES detector. The table gives the equatorial coordinates, the angular error estimate $\beta_{\rm IC}$ of the event, and the 90% C.L. upper limits on the flux $\Phi_0^{90\%}$ (in units of 10^{-8} GeV cm^{-2} s^{-1}).

HESE ID	$\delta[^\circ]$	$\alpha[^\circ]$	$\beta_{\rm IC}[^\circ]$	$\Phi_0^{90\%}$
3	−31.2	127.9	1.4	2.1
5	−0.4	110.6	1.2	1.5
8	−21.2	182.4	1.3	1.7
13	40.3	67.9	1.2	2.4
18	−24.8	345.6	1.3	2.0
23	−13.2	208.7	1.9	1.7
28	−71.5	164.8	1.3	1.2
37	20.7	167.3	1.2	1.7
38	14.0	93.3	1.2	2.1
43	−22.0	206.6	1.3	1.3
44	0.0	336.7	1.2	1.8
45	−86.3	219.0	1.2	1.2
53	−37.7	239.0	1.2	1.6

non-negligible angular error estimate, the direction parameters are not fixed but rather fitted within a cone of twice their angular error estimate around the direction given by the IceCube tracks. The coordinates of these events are shown in Table IV together with their angular uncertainty (provided by the IceCube Collaboration), fitted number of signal events, and upper limits on the flux derived from this analysis.

The muon track candidate from the HESE sample with the largest excess in fitted signal is the IceCube track with ID 3 and $\mu_{\rm sig} = 5.3$. The fitted cluster is located at $(\alpha, \delta) = (130.1^\circ, -29.8^\circ)$, which is at a distance of 1.5° from the original HESE track at $(\alpha, \delta) = (127.9^\circ, -31.2^\circ)$. The observed post-trial p-value is 20% (significance of 1.2σ). The upper limit on the signal from this candidate is $\Phi_0^{90\%} = 2.1 \times 10^{-8}$ GeV cm^{-2} s^{-1}. The cluster is shown in the middle left panel of Fig. 8.

C. Galactic Center region

The restricted search region is defined as an ellipse around the Galactic Center with semiaxes of 20° in Galactic longitude and 15° in Galactic latitude. Due to the smaller search area, the search for astrophysical sources is more sensitive than a full-sky search because it is less probable for background events to randomly cluster together, mimicking the signature of a signal. Assuming the usual E^{-2} spectrum, the most significant cluster found in this restricted region is located at $(\alpha, \delta) = (257.4^\circ, -41.0^\circ)$ with a pre-trial p-value of 0.09% and a fitted number of signal events of 2.3. The post-trial significance of this cluster—calculated as in the full-sky search but in the restricted region around the Galactic Center—is 60%. Other spectral indices ($\gamma = 2.1,\ 2.3,\ 2.5$) and source extensions ($\sigma = 0.5^\circ,\ 1.0^\circ,\ 2.0^\circ$) are considered, yielding different most-significant clusters. The source extension is quantified by the σ of the Gaussian distribution. For a spectral index of $\gamma = 2.5$ and a point source, the most significant cluster is found at $(\alpha, \delta) = (273.0^\circ, -42.2^\circ)$, with a pre-trial p-value of 0.02% and a post-trial significance of 30%. The distributions of events for these two clusters are shown in the middle right and bottom left panels of Fig. 8, respectively. The positions of the most significant clusters found for the remaining spectral indices and source extensions considered are within 1° of the position of the latter.

The declination-dependent limit of such a restricted point-like source search is shown in Fig. 10, both for different energy spectral indices γ and different source extensions. The upper limits increase with increasing values of γ and with the source extension. A softer energy spectrum of cosmic neutrinos (larger values of the spectral index γ) is less distinguishable from the spectrum of atmospheric neutrinos, as is a source with a larger extension. For a softer spectrum, fewer neutrinos are emitted by the source within an energy range in which they can be statistically separated from atmospheric neutrinos. The flux

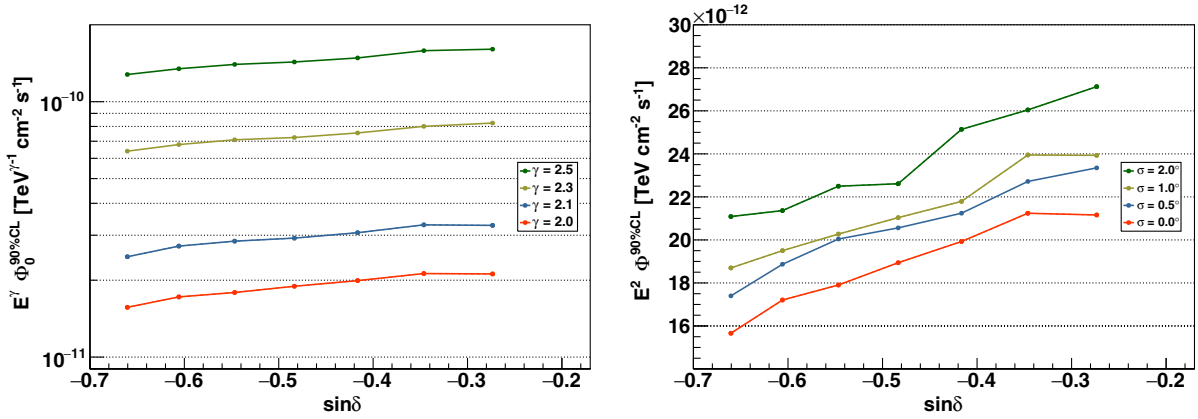

FIG. 10. 90% C.L. upper limits of a search restricted to the region around the origin of the Galactic coordinates at $(\alpha, \delta) = (266.40^\circ, -28.94^\circ)$ assuming different spectral indices for the neutrino flux (left) and different source extensions for $\gamma = 2$ (right).

required at the normalization point for a significant detection is therefore larger.

D. Sagittarius A*

Supermassive black holes are strong candidates for accelerators of very-high energy cosmic rays and therefore for cosmic neutrino production [34]. Additionally, due to the high concentration of candidate sources and gas around the Galactic Center, it is probable that an extended signal from that region will be detected before identifying individual point-like sources. For this reason, Sagittarius A*, located at $(\alpha, \delta) = (266.42°, -29.01°)$, is investigated as an extended source with widths between 0.5° and 5°. The cluster of events around Sagittarius A* reconstructed by ANTARES is shown in the bottom right panel of Fig. 8. The sensitivity and upper limits when assuming different source extensions can be seen in Fig. 11. The sensitivity degrades with increasing extension, but an improvement of up to a factor of 2.7 can be achieved by assuming an extended source with the simulated extension. The largest excess above the background is found at an extension of 0° with a pre-trial p-value of 22%.

V. SYSTEMATIC UNCERTAINTIES

The effects of systematic uncertainties on the absolute pointing accuracy, angular resolution, acceptance, and background rate distribution of events are evaluated.

Absolute pointing accuracy uncertainty: Uncertainties of 0.13° and 0.06° on the horizontal (ϕ) and vertical (θ) directions, respectively, was established in a previous study [35]. To take this into account, randomly generated offsets have been added to the ϕ and θ variables of the simulated events. The offsets are generated according to two Gaussian distributions with the aforementioned uncertainties as sigmas.

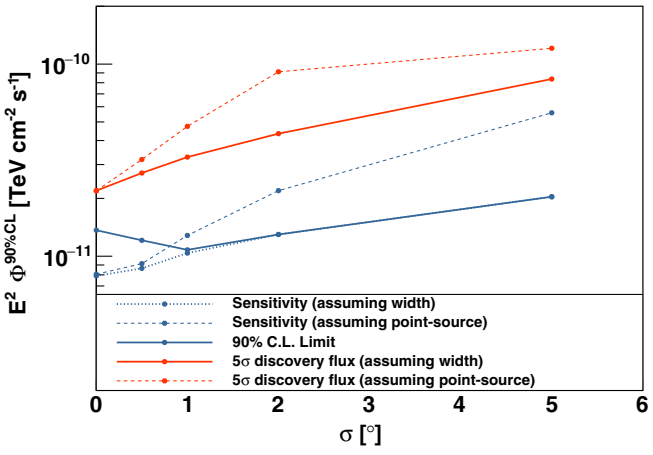

FIG. 11. Discovery flux (dotted red), median sensitivity (dotted blue), and 90% C.L. upper limits (green) for a search for an extended source at Sagittarius A* at $(\alpha, \delta) = (266.42°, -29.01°)$ assuming different angular extensions σ. The dashed lines correspond to the point-like source assumption.

Angular resolution uncertainty: The angular resolution of the track reconstruction algorithm can be affected by the accuracy of the detected hit times. A smearing of these times was performed in simulations, leading to a 15% degradation on the angular resolution in the track channel [15]. For neutrinos of the shower sample, the reconstruction of the direction depends most significantly on the recorded charge. A smearing in the measured charges [36] leads to a 12% degradation of the angular resolution for the shower channel.

Acceptance uncertainty: A 15% uncertainty on the acceptance has been considered for the calculation of the reported fluxes. This uncertainty was calculated after performing simulations with a reduction of the OM efficiency by 15% [15].

Background uncertainty: In order to account for possible systematic uncertainties on the background, the distributions of the background rates in Fig. 4 are parametrized by two different spline functions: $R(\delta)$ and $B(\delta)$ (the red and blue lines). The declination-dependent distribution of background events of the pseudoexperiments is determined as $\mathcal{B}(\delta) = B(\delta) + r \cdot (R(\delta) - B(\delta))$, with r being a random number drawn for each pseudoexperiment from a uniform distribution between -1 and 1.

It is found that not considering these uncertainties would improve the median sensitivity at 90% C.L. and the 5σ discovery potential by less than 5%.

VI. CONCLUSION AND OUTLOOK

Various searches for cosmic neutrino sources using combined information from the track and shower channels have been presented. These searches provide the most sensitive limits for a large fraction of the southern sky, especially at neutrino energies below 100 TeV. No significant evidence of cosmic neutrino sources has been found. The IceCube HESE accumulation reported near the Galactic Center could not be totally attributed to either a point-like source or an extended source.

The most significant cluster in the full-sky search is located at $(\alpha, \delta) = (343.8°, 23.5°)$ with a post-trial significance of 5.9% or 1.9σ.

Upper limits on the neutrino flux from 106 astrophysical candidates and 13 IceCube muon tracks have been presented. The most significant source candidate is HESSJ0632 + 057—located at $(\alpha, \delta) = (98.24°, 5.81°)$, with a post-trial significance of 1.5σ. The upper limit on the signal from this candidate is $E^2 d\Phi/dE = 2.40 \times 10^{-8}$ GeV cm^{-2} s^{-1}.

The most significant cluster of events close to the Galactic Center when assuming a point-like source with a E^{-2} energy spectrum is located at $(\alpha, \delta) = (-102.6°, -41.0°)$ with a post-trial p-value of 60%.

Sagittarius A* has been investigated as a possible extended source. Upper limits for the flux and number

of events assuming a Gaussian morphology with different extensions have been presented. The largest excess over the background is observed at an angular extension of 0° with a pre-trial p-value value of 22%.

The KM3NeT/ARCA neutrino telescope [37], which is currently under construction, will combine a cubic-kilometer-sized detector with the same high visibility towards the Galactic Center as ANTARES. It is expected that this detector will be able to make definite statements about a neutrino flux from several Galactic candidates within a few years of operation.

ACKNOWLEDGMENTS

The authors acknowledge the financial support of the funding agencies: Centre National de la Recherche Scientifique (CNRS), Commissariat à l'énergie atomique et aux énergies alternatives (CEA), Commission Européenne (FEDER fund and Marie Curie Program), Institut Universitaire de France (IUF), IdEx program and UnivEarthS Labex program at Sorbonne Paris Cité (ANR-10-LABX-0023 and ANR-11-IDEX-0005-02), Labex OCEVU (ANR-11-LABX-0060) and the A*MIDEX project (ANR-11-IDEX-0001-02), Région Île-de-France (DIM-ACAV), Région Alsace (contrat CPER), Région Provence-Alpes-Côte d'Azur, Département du Var and Ville de La Seyne-sur-Mer, France; Bundesministerium für Bildung und Forschung (BMBF), Germany; Istituto Nazionale di Fisica Nucleare (INFN), Italy; Stichting voor Fundamenteel Onderzoek der Materie (FOM), Nederlandse organisatie voor Wetenschappelijk Onderzoek (NWO), the Netherlands; Council of the President of the Russian Federation for young scientists and leading scientific schools supporting grants, Russia; National Authority for Scientific Research (ANCS), Romania; Ministerio de Economía y Competitividad (MINECO): Plan Estatal de Investigación (refs. FPA2015-65150-C3-1-P, -2-P and -3-P, (MINECO/FEDER)), Severo Ochoa Centre of Excellence and MultiDark Consolider (MINECO), and Prometeo and Grisolía programs (Generalitat Valenciana), Spain; Ministry of Higher Education, Scientific Research and Professional Training, Morocco. We also acknowledge the technical support of Ifremer, AIM and Foselev Marine for the sea operation and the CC-IN2P3 for the computing facilities.

APPENDIX: SHOWER SELECTION CUT PARAMETERS

In this appendix, we provide additional details concerning some of the parameters referred to in Table II used to define selection criteria for the shower channel events.

*Interaction vertex:*Reconstructing atmospheric muons with a shower algorithm often results in reconstructed vertex positions that lie far away from the instrumented volume of the detector. This can be approximated with a cylindrical structure with a height of 350 m and a radius of 180 m. Cuts on the radial distance of the reconstructed shower position from the vertical axis of the detector ($R_{sh} < 300$ m) and on the vertical distance above the center of the detector ($|Z_{sh}| < 250$ m) are applied.

*RDF:*A different shower reconstruction algorithm was originally developed for diffuse flux analyses [19]. Among all available quality parameters provided by this reconstruction chain, a subset of five parameters that showed a high potential to separate atmospheric muon tracks from shower events was chosen as input in a *RDF* classification. The distribution of the *RDF* parameter for cosmic neutrinos and atmospheric muons and neutrinos after applying the cuts prior to the *RDF* cut is shown in the left panel of Fig. 12. Only shower events with $RDF > 0.3$ are used in this analysis.

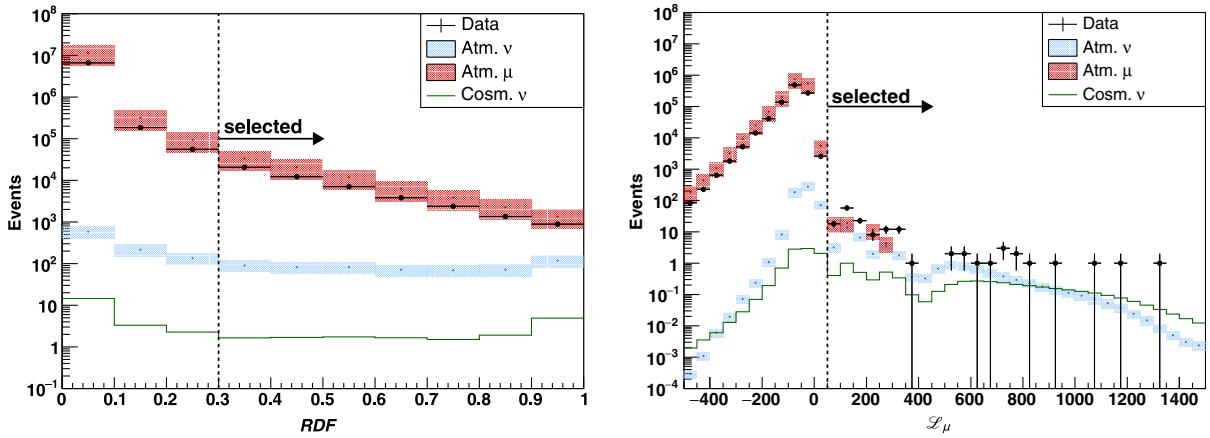

FIG. 12. Left: *RDF* parameter for data, cosmic neutrinos, and atmospheric background. This figure corresponds to the event distributions after all the cuts prior to the *RDF* listed in Table II. Right: Muon likelihood ratio parameter for data, cosmic neutrinos, and atmospheric background. This figure corresponds to the event distributions after the *RDF* and all previous cuts listed in Table II. In both panels the dashed vertical line indicates the cut value.

Muon likelihood: An additional likelihood function has been developed to discriminate between neutrinos that produce showers and the background of atmospheric muons. This likelihood considers only hits that coincide with another hit on the same Storey (which contains a triplet of PMTs at the same position in the detector line) within 20 ns. Its probability density function is based on the time residual t_{res} of the hits (time difference between the detected and expected hits from the assumption of a point-like light emission from the simulated vertex position without photon scattering), the number N of on-time hits (-20 ns $< t_{\mathrm{res}} < 60$ ns), and the distance d of the hits to the reconstructed shower position. Thus the parameter that distinguishes between showers and muons is

$$\mathcal{L}_{\mu} = \sum_{\mathrm{Hits}} \log\{P_{\mathrm{sig}}/P_{\mathrm{bkg}}\},$$

with $P_{\mathrm{sig}} = P(N, d, t_{\mathrm{res}}|\nu)$ and $P_{\mathrm{bkg}} = P(N, d, t_{\mathrm{res}}|\mu)$.

The distribution for this quantity plotted for atmospheric muons and cosmic showers after all cuts prior to the muon likelihood cut is shown in the right panel of Fig. 12. Shower events with $\mathcal{L}_{\mu} < 50$ are excluded from the analysis. This method further reduces the number of atmospheric muons by more than 2 orders of magnitude.

[1] T. K. Gaisser, F. Halzen, and T. Stanev, Phys. Rep. **258**, 173 (1995); **271**, 355(E) (1996).
[2] F. Halzen and D. Hooper, Rep. Prog. Phys. **65**, 1025 (2002).
[3] J. K. Becker, Phys. Rep. **458**, 173 (2008).
[4] S. R. Kelner and F. A. Aharonian, Phys. Rev. D **78**, 034013 (2008); **82**, 099901(E) (2010).
[5] K. Murase, AIP Conf. Proc. **1666**, 040006 (2015).
[6] T. Michael (ANTARES Collaboration) *Proc. Sci.*, ICRC2015 (2016) 1078.
[7] A. Albert *et al.* (ANTARES Collaboration), arXiv:1708.03649.
[8] M. Ageron *et al.* (ANTARES Collaboration), Nucl. Instrum. Methods Phys. Res., Sect. A **656**, 11 (2011).
[9] Y. Becherini, A. Margiotta, M. Sioli, and M. Spurio, Astropart. Phys. **25**, 1 (2006).
[10] G. Carminati, A. Margiotta, and M. Spurio, Comput. Phys. Commun. **179**, 915 (2008).
[11] J. Brunner (ANTARES Collaboration), in *Technical Aspects of a Very Large Volume eutrino Telescope in the Mediterranean Sea. Proceedings, Workshop, VLVnuT Workshop, Amsterdam, Netherlands, October 5–8, 2003*, edited by E. de Wolf (NIKHEF, Amsterdam, 2004), p. 109.
[12] A. Margiotta (ANTARES Collaboration), Nucl. Instrum. Methods Phys. Res., Sect. A **725**, 98 (2013).
[13] V. Agrawal, T. K. Gaisser, P. Lipari, and T. Stanev, Phys. Rev. D **53**, 1314 (1996).
[14] L. A. Fusco and A. Margiotta (ANTARES Collaboration), Eur. Phys. J. Web Conf. **116**, 02002 (2016).
[15] S. Adrian-Martinez *et al.* (ANTARES Collaboration), Astrophys. J. **760**, 53 (2012).
[16] S. Adrian-Martinez *et al.* (ANTARES Collaboration), Astrophys. J. **786**, L5 (2014).
[17] F. Schssler (ANTARES Collaboration), in *Proceedings, 33rd International Cosmic Ray Conference (ICRC2013), Rio de Janeiro, Brazil, July 2–9, 2013*, edited by R. C. Shellard (Centro Brasileiro de Pesquisas Fisicas, Rio de Janeiro, 2014), p. 0421.
[18] S. Adrian-Martinez *et al.* (ANTARES Collaboration), Eur. Phys. J. C **73**, 2606 (2013).
[19] A. Albert *et al.* (ANTARES Collaboration), Eur. Phys. J. C **77**, 419 (2017).
[20] M. G. Aartsen *et al.* (IceCube Collaboration), Phys. Rev. Lett. **113**, 101101 (2014).
[21] C. Kopper, W. Giang, and N. Kurahashi (IceCube Collaboration), *Proc. Sci.*, ICRC2015 (2016) 1081.
[22] A. Abramowski *et al.* (H.E.S.S. Collaboration), Nature (London) **531**, 476 (2016).
[23] M. G. Aartsen *et al.* (IceCube Collaboration), Astrophys. J. **833**, 3 (2016).
[24] J. Neyman, Phil. Trans. R. Soc. A **236**, 333 (1937).
[25] M. G. Aartsen *et al.* (IceCube Collaboration), Astrophys. J. **835**, 151 (2017).
[26] M. G. Aartsen *et al.* (IceCube Collaboration), Astrophys. J. **824**, L28 (2016).
[27] S. P. Wakely and D. Horan, in *Proceedings, 30th International Cosmic Ray Conference (ICRC 2007), Merida, Yucatan, Mexico, July 3–11, 2007*, edited by R. Caballero, J. C. D'Olivo, G. Medina-Tanco, L. Nellen, F. A. Sanchez, and J. F. Valdes-Galicia (Universidad Nacional Autonoma de Mexico, Mexico City, Mexico, 2008), p. 1341.
[28] A. U. Abeysekara *et al.*, Astrophys. J. **843**, 40 (2017).
[29] F. Krau *et al.*, Astron. Astrophys. **566**, L7 (2014).
[30] M. Kadler *et al.*, Nat. Phys. **12**, 807 (2016).
[31] S. Adrian-Martinez *et al.* (ANTARES Collaboration), Astron. Astrophys. **576**, L8 (2015).
[32] S. Adrian-Martinez *et al.* (ANTARES Collaboration), J. Cosmol. Astropart. Phys. 11 (**2014**) 017.
[33] A. L. Read, in *Workshop on Confidence Limits, CERN, Geneva, Switzerland, January 17–18, 2000*, edited by L. Lyons, Y. Perrin, and F. E. James (CERN, Geneva, 2000), p. 81.
[34] Y. Bai, A. J. Barger, V. Barger, R. Lu, A. D. Peterson, and J. Salvado, Phys. Rev. D **90**, 063012 (2014).
[35] S. Adrian-Martinez *et al.* (ANTARES Collaboration), J. Instrum. **7**, T08002 (2012).
[36] J. A. Aguilar *et al.* (ANTARES Collaboration), Nucl. Instrum. Methods Phys. Res., Sect. A **622**, 59 (2010).
[37] S. Adrian-Martinez *et al.* (KM3NeT Collaboration), J. Phys. G **43**, 084001 (2016).